Materials Today Energy 34 (2023) 101301

Contents lists available at ScienceDirect

Materials Today Energy

journal homepage: www.journals.elsevier.com/materials-today-energy/

Extending the high-voltage operation of Graphite/NCM811 cells by constructing a robust electrode/electrolyte interphase layer

Wengao Zhao [a, f, g, *], Kuan Wang [b, g], Romain Dubey [c, d], Fucheng Ren [e], Enzo Brack [a], Maximilian Becker [a], Rabeb Grissa [a], Lukas Seidl [a], Francesco Pagani [a], Konstantin Egorov [a], Kostiantyn V. Kravchyk [c, d], Maksym V. Kovalenko [c, d], Pengfei Yan [b], Yong Yang [e], Corsin Battaglia [a]

[a] Materials for Energy Conversion, Empa-Swiss Federal Laboratories for Materials Science and Technology, 8600, Dübendorf, Switzerland
[b] Beijing Key Laboratory of Microstructure and Properties of Solids, Faculty of Materials and Manufacturing, Beijing University of Technology, Beijing, 100124, China
[c] Laboratory for Thin Films and Photovoltaics, Empa-Swiss Federal Laboratories for Materials Science and Technology, 8600, Dübendorf, Switzerland
[d] Laboratory of Inorganic Chemistry, Department of Chemistry and Applied Biosciences, ETH Zürich, Zürich, CH-8093, Switzerland
[e] College of Energy, Xiamen University, Xiamen, 361005, Fujian, PR China

ARTICLE INFO

Article history:
Received 17 January 2023
Received in revised form
27 February 2023
Accepted 17 March 2023
Available online 6 April 2023

Keywords:
High-voltage cycling stability
LiF-riched
Transition metal dissolution
Cation-disordered

ABSTRACT

The cycling life of layered Ni-rich $LiNi_{1-x-y}Co_xMn_yO_2$ (NCM, 1-x-y $\geq$ 0.8) is typically extended by restricting the upper cut-off voltage during cycling to below 4.2 V, sacrificing, however, the untapped additional capacity above the cut-off voltage. To make this additional capacity available, we investigate graphite/$LiNi_{0.8}Co_{0.1}Mn_{0.1}O_2$ cells cycled to high upper cut-off voltages up to 4.5 V at high electrode areal capacities of 4.8 mAh/cm^2 in a standard electrolyte consisting of 1 M lithium hexafluorophosphate ($LiPF_6$) in ethylene carbonate and ethylene methyl carbonate (ethylene carbonate:ethylene methyl carbonate = 3:7 vol% + 2% vinylene carbonate). Although the initial capacity reaches 190 mAh/g, the capacity retention after 300 cycles to 4.5 V is only 66%. Employing a combination of tris(trimethylsilyl) phosphite and lithium difluoro(oxalato)borate as electrolyte additives, we demonstrate excellent capacity retention of 85% after 300 cycles to 4.5 V. Moreover, graphite/$LiNi_{0.8}Co_{0.1}Mn_{0.1}O_2$ cells with additives show improved capacity retention also at elevated temperatures of 60 °C. A detailed post-mortem analysis reveals the formation of a compact and LiF-rich and B-containing cathode/electrolyte interphase layer on the $LiNi_{0.8}Co_{0.1}Mn_{0.1}O_2$ particles cycled with tris(trimethylsilyl)phosphite and lithium difluoro(oxalato)borate additives, substantially suppressing the transition metal dissolution and the cation-disordered layer formation on the exposed particles' surface.

1. Introduction

Lithium-ion batteries based on graphite and Ni-rich $LiNi_{1-x-y}Co_xMn_yO_2$ (NCM) with 1-x-y $\geq$ 0.8 represent a key enabling technology for the transition to electric mobility and the integration of renewables into the grid [1–4]. However, when charged to a high cell voltage, Ni-rich NCM exhibits high surface reactivity leading to parasitic reactions with the electrolyte and dramatic lattice volume changes that can exceed 6% and provoke particle cracking [5–7]. For this reason, graphite/NCM cells are typically cycled to an upper cut-off voltage of less than 4.2 V [8]. It is still challenging to attain high-capacity retention with graphite/NCM full cells at high voltage operation due to the finite Li reservoir provided exclusively by the cathode. Therefore, it is necessary to minimize the depletion of the electrochemically active Li inventory by forming a stable electrode/electrolyte interphase.

Various strategies have been employed to improve the high-voltage cycling stability of Ni-rich NCM cathodes. Protective coatings applied to the NCM particle surface are intended to prevent

* Corresponding author.
E-mail address: wengao.zhao@kit.edu (W. Zhao).
[f] Dr. W. Zhao fooNow at Battery and Electrochemistry Laboratory (BELLA), Institute of Nanotechnology, Karlsruhe Institute of Technology (KIT), Hermann-von-Helmholtz-Platz 1, 76,344 Eggenstein-Leopoldshafen, Germany.
[g] W. Zhao and K. Wang contributed equally.

https://doi.org/10.1016/j.mtener.2023.101301

direct contact with an electrolyte. However, protective coatings tend to become ineffective during long-term cycling to high cell voltages when particles crack [9–12]. Doping of NCM particles, e.g. by Al or Ti, can improve the tolerance of particles against cracking [1,13–15]. Dopants can be introduced during NCM (a hydroxide precursor) particle synthesis or via a high-temperature solid-state diffusion step after the synthesis, wherein it is not easy to precisely control the dopant position and to distinguish the individual effects of individual lattice dopants [16,17]. The formation of a passivating cathode/electrolyte interphase (CEI) layer employing sacrificial electrolyte additives is one of the most effective and economical methods for improving the electrochemical performance of high-voltage cathodes by forming a robust and lithium-ion conductive CEI layer to block the electron transport and allow Li^+ access. Some of additives are beneficial to suppress the catalytic decomposition of the carbonate electrolyte by forming a robust CEI layer, while others may help to effectively suppress transition metal dissolution and following the electrode cross-talk as well as prevent the concomitant failure cascade [18–25]. Tris(trimethylsilyl)phosphite (TMSPi) was shown to act as an effective scavenger for hydrofluoric acid, preventing the acidification of the electrolyte. TMSPi not only reduces transition metal dissolution from the NCM particles but also prevents depletion of the electrochemically active Li inventory through the formation of Li-containing deposits, thereby extending the cycle life of graphite/NCM811 cells [26–29]. However, TMSPi is continuously consumed to react with hydrofluoric acid during high-voltage operation, which is a negative factor to obtain excellent long-term cycling stability. Therefore, it is necessary to integrate an additional additive to assist TMSPi to achieve superior long-term cycling stability at high voltage operation by forming a more compact CEI layer and suppressing the phase transformation on the surface of the NCM cathode [21,27]. As a borate-containing additive, lithium difluoro(oxalato)borate (LiDFOB) is beneficial to improve the cycling stability at a high cell voltage through preferential decomposition to form a stable and lithium-ion-conducting CEI layer. The resulting borate-containing and LiF-enriched CEI layer was shown to be robust during high-voltage and high-temperature operation [27,30–33].

In this study, we explore the complementary synergistic effects of TMSPi and LiDFOB via a detailed post-mortem analysis demonstrating a graphite/NCM811 cell with excellent capacity retention of 85% after 300 cycles to a high upper cut-off voltage of 4.5 V. A robust and high-voltage stable CEI layer is formed on the cycled cathode containing LiF-rich and B-containing species, substantially suppressing the transition metal dissolution and the cation-disordered layer formation on the exposed NCM811, thereby significantly enhancing the cycling stability of the graphite/NCM811 cells cycled to an upper cut-off voltage of 4.5 V.

2. Experimental section

2.1. Materials preparation

$Ni_{0.8}Co_{0.1}Mn_{0.1}(OH)_2$ precursor particles were synthesized in a continuously stirred 3 L reaction tank by co-precipitation under a nitrogen gas atmosphere. A 2 mol/L mixed solution of $NiSO_4 \cdot 6H_2O$, $CoSO_4 \cdot 7H_2O$, and $MnSO_4 \cdot H_2O$ (molar ratio of Ni: Co: Mn = 8 : 1: 1) was fed into the tank, while maintaining the pH at 11.2. The temperature of the tank was kept constant at 50 °C. During co-precipitation, an 8 mol/L NaOH solution (precipitator agent) and a 5 mol/L $NH_3 \cdot H_2O$ solution (chelating agent) were simultaneously injected. The collected precursor was washed 3 times with distilled water to eliminate residual chemicals and then was dried in an oven for 8 h at 120 °C. Cathode particles were synthesized from the hydroxide precursor particles through mixing the $Ni_{0.8}Co_{0.1}Mn_{0.1}(OH)_2$ with $LiOH \cdot H_2O$ in a molar ratio of M:Li = 1:1.03 and sintering at 500 °C for 10 h and 750 °C for 15 h, respectively. Low mass loading electrodes were fabricated by tape casting on an aluminum current collector foil (15 mm) using a slurry consisting of a 90 wt%, 5 wt% carbon black, and 5 wt% Poly(vinylidene fluorid) (PVDF) binder in N-methylpyrrolidone with a nominal wet coating thickness of 100 μm. High-mass-loading electrodes were fabricated by tape casting on an aluminum current collector foil (15 μm) using a slurry consisting with a 96 wt%, 2 wt% carbon black, and 2 wt% PVDF binder in N-methylpyrrolidone with a nominal wet coating thickness of 220 μm. The obtained cathode electrodes were dried in a vacuum oven at 120 °C, while the low mass loading electrode and high mass loading electrode were calendared to 30–40 μm and 120 μm, respectively.

Carbon-coated graphite (C-Nergy, Imerys, 7.25 g) and carbon black (Super P, Imerys, 0.053 g) were mixed in a 50 mL zirconia ball mill jar and ball milled at 300 rpm for 30 min. To this dry mixture, a solution of carboxymethyl cellulose (CMC, Sunrose MAC 500LC, Nippon Paper Group, 0.095 g) in Milli-Q water (11.75 mL) was added and the slurry was ball milled at 300 rpm for 3 h. To this slurry, JSR TRD 102A (0.150 g of a 48 wt% suspension in water) was added. The resulting mixture, consisting of 96.05% graphite +0.7% carbon black +3.25% binder (CMC + JSR TRD 102A), was mixed with a magnetic stirrer for 5 min to yield a homogeneous slurry, which was coated onto a clean Cu foil (12 μm) via doctor-blading at a speed of 4 mm/s. The obtained graphite electrodes were dried overnight under air and calendared stepwise in 3–5 steps from ~200 μm down to the target density (~1.5 g/cm^3). The active material loading was ca. 14.9 mg/cm^2 for an areal capacity of ca. 5.2 mAh/cm^2.

2.2. Cell assembly and cycling

The electrochemical performance of the NCM811 cathode was evaluated using CR2032-type coin cells with Al-clad positive cases from MTI. For Li/NCM811 half-cell tests, the low mass loading, NCM811, is employed, while the graphite/NCM811 full cells used the high mass loading of the NCM811 electrode with 24 mg/cm^2 and the paired graphite electrode with an areal capacity of 5.2 mAh/cm^2, and thus the N/P ratio is about 1.08. The cathode electrodes were punched into disks with a diameter of 12 mm, while the Li metal anode and graphite anode were punched into disks with a diameter of 15 mm. Coin cells were assembled in an argon-filled glovebox (MBraun). The cells contained one NCM811 electrode as the cathode, a lithium disk or graphite electrode as the anode, a Celgard 2500 separator, and 100 μl baseline electrolyte (1 M $LiPF_6$ in EC (ethylene carbonate): ethylene methyl carbonate (EMC) (3:7 vol%) + 2% vinylene carbonate (VC) (in full cell)), a baseline electrolyte with a single additive (1% wt TMSPi or 2% wt LiDFOB), or a baseline electrolyte with dual-additives (1% wt TMSPi + 2% wt LiDFOB). Galvanostatic cycling of the coin cells was performed on a Biologic BCS-805 multichannel potentiostat and/or an Arbin battery cell tester with the cells located in a climate chamber at a constant temperature of 25 °C or 60 °C. The graphite/NCM811 cells were tested in the voltage range of 2.5–4.35/4.5V with a 0.2C/0.5C charge/discharge protocol, and a constant voltage charging protocol was applied at the end of the charge cut-off voltage until the current density decreases to 0.05C (1C = 180 mA/g). The electrochemical impedance spectra were measured during charging at a cell voltage of 4.2 V using a Biologic BCS multichannel potentiostat. The frequency varied from 100 kHz to 10 mHz with an amplitude of 10 mV.

2.3. Material characterization

The morphology of particles and electrodes was characterized by scanning electron microscopy (SEM, FEI Nano SEM230).

Electrode cross-sections were fabricated using a broad-ion beam mill (Hitachi IM400 plus). To avoid the melting of the PVDF binder, samples were cooled to −50 °C before as well as during the process of milling. The crystal structure of NCM811 was characterized by X-ray diffraction (XRD, Panalytical XPert Pro). Samples for transmission electron microscopy (TEM) were prepared by a focused-ion beam (FIB, FEI Helios Dual-Beam). Scanning TEM (STEM)-high-angle annular dark-field imaging and STEM-energy dispersive X-ray spectroscopy mapping were performed on a FEI Titan 60−300 microscope at 300 kV. The detector collects electrons within a range of 58.5−200 mrad for high-angle annular dark-field imaging imaging. The CEI composition on the surface of cycled NMC811 cathodes was analyzed using X-ray photoelectron spectroscopy (XPS) on a PHI Quantum 2000 with a pass energy of 30 eV. The cycled electrode was harvested from the cycled cells and washed three times with a dimethyl carbonate solvent and was characterized using XPS and TEM. The elemental composition of the SEI on the cycled graphite electrodes was further characterized by time-of-flight secondary ion mass spectrometry (TOF-SIMS, ION-TOF) using a pulsed 25 keV Bi^+ primary ion beam. Density functional theory (DFT) calculations were employed to estimate the energies of the highest occupied molecular orbital (HOMO) and lowest unoccupied molecular orbital (LUMO) of all electrolyte components (EC, EMC, $LiPF_6$, LiDFOB and TMSPi).

3. Results and discussions

In Fig. 1, we show SEM images of NCM811 electrodes, XRD patterns of NCM811 particles, as well as the cycling performance of Li/NCM811 half cells. In Fig. 1a–c, the cross-section SEM images clearly indicate a round particle morphology with an average particle diameter of ~10 μm. The particles hardly show any intra-particle porosity, suggesting that very dense particles were synthesized, which is beneficial for achieving good cycling stability [34]. The XRD pattern in Fig. 1d indicates the formation of a highly ordered layered structure witnessed by an intensity ratio of the (003)/(104) reflections being higher than 1.2. Moreover, the two twin reflections of (006)/(102) and (108)/(110) are clearly split, further confirming the R $\bar{3}$ m-layered structure (Fig. 1e and f).

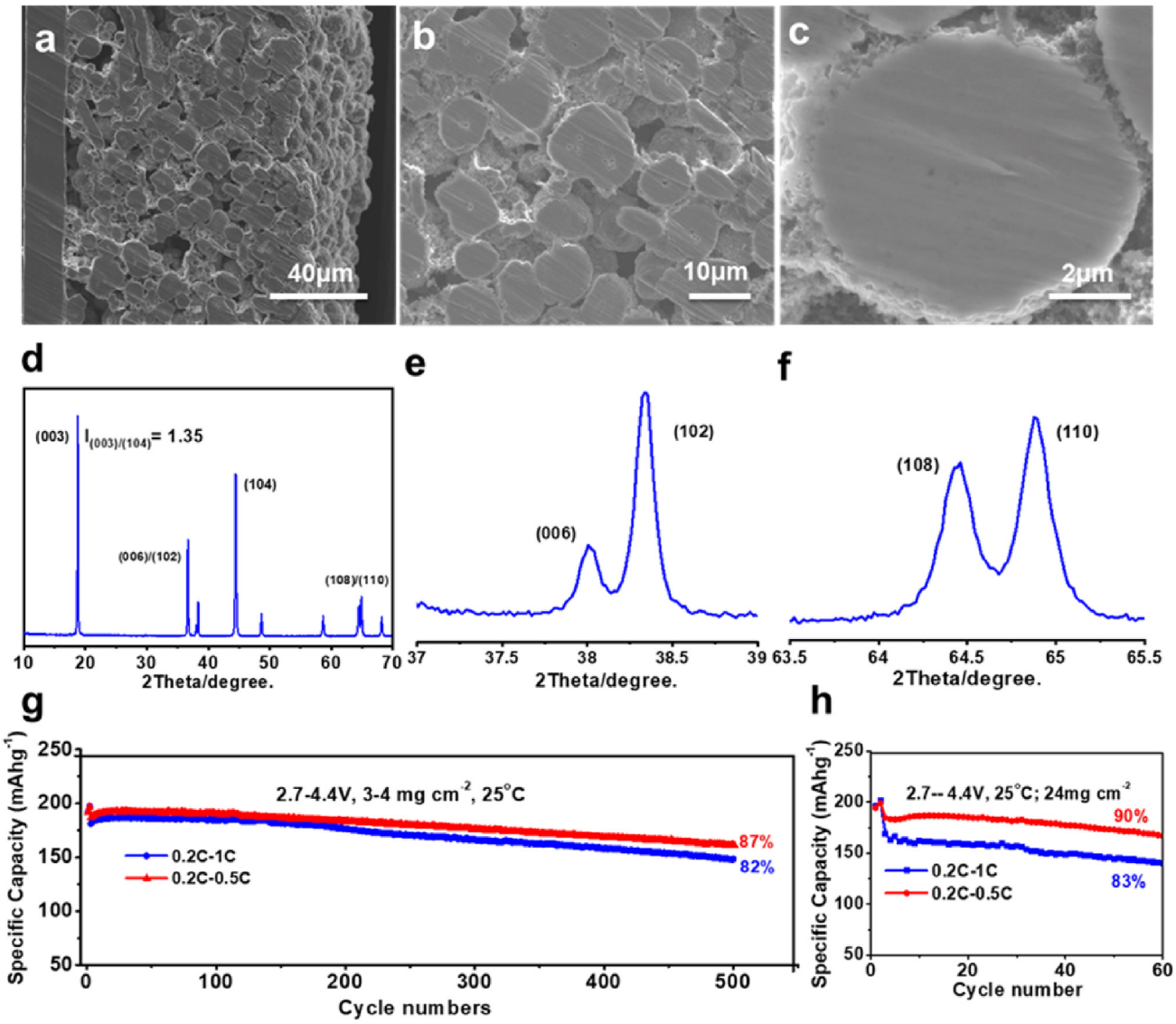

Fig. 1. (a–c) Cross-section SEM images of the 4.8 mAh/cm^2 NCM811 electrode. (d–f) XRD patterns and split peaks of (006)/(102) and (108)/(110) facets. Cycling performance of Li/NCM811 half cells with (g) low (3–4 mg/cm^2) and (h) high (24 mg/cm^2) mass loading NCM811 electrodes. SEM, scanning electron microscopy; XRD, X-ray diffraction.

We tested the cycling performance of Li/NCM811 half cells with an average mass loading (3–4 mg/cm^2) and a high mass loading (24–25 mg/cm^2). At a low mass loading of 3–4 mg/cm^2, the Li/NCM811 cells deliver very promising cycling stability in the voltage range of 2.7–4.4V and at 25 °C. In Fig. 1g, both cells show a high initial specific capacity of 186 mAh/g vs. 181 mAh/g and capacity retention of 87% vs. 82% at 0.2C/0.5C and 0.2C/1C charging/discharging, respectively. A rate performance assessment is also conducted with 5 cycles at 0.1C/0.1C charging/discharging and applying at 0.2C charging and 0.2C–10C discharging, indicating a good discharge rate performance as the cell still maintains 80% of the initial capacity obtained when cycled at 0.2C/10C charging/discharging (Fig. S1). At a high mass loading of 24 mg/cm^2, shown in Fig. 1h, the Li/NCM811 cells show capacity retention of 90% and 83% after 60 cycles at 0.2C/0.5C and 0.2C/1C. The relatively lower cycling stability is attributed to the instability of the Li metal anode towards the Li metal dendrite formation when paired with high mass loading cathodes, resulting in high current densities [35,36].

In order to evaluate the cycling stability at a practical areal capacity in full cells, we paired the NCM811 cathodes with a high areal capacity of 4.8 mAh/cm^2 (24 mg/cm^2 x 200 mAh/g) and a graphite anode with a high areal capacity of 5.2 mAh/cm^2 (14.9 mg/cm^2 x 350 mAh/g). Remarkably, the cell with the baseline electrolyte displays high-capacity retention of 78% after 500 cycles at 0.2C/0.5C charging/discharging to an upper cut-off voltage of 4.35 V. Moreover, the cell using both LiDFOB and TMSPi additives delivers higher capacity retention of 85% than the cell using only a LiDFOB (81%) or TMSPi (79%) additive under the same cycling conditions. The related charge/discharge profiles are shown in Fig. S2, indicating the less pronounced evolution of charge/discharge curves in the cell using additives. Considering that currently the standard requirements for Ni-rich NCM for automotive applications are to

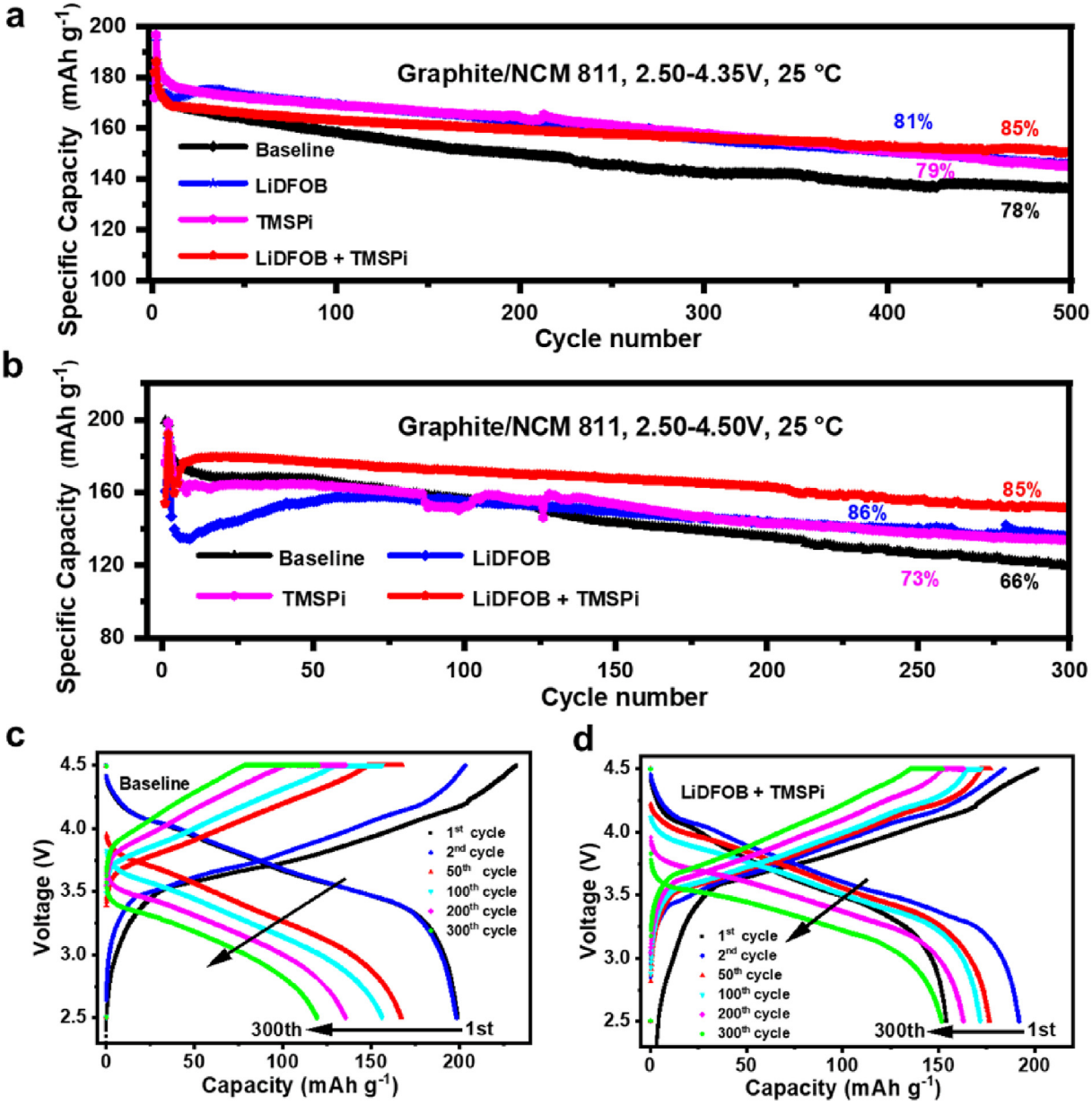

Fig. 2. Long-term cycling of the graphite/NCM811 cells using high mass loading electrodes and different electrolytes in the voltage ranges 2.5–4.35 V (a) and 2.5–4.5 V (b). The charge/discharge profiles of the graphite/NCM811 cells in the voltage range 2.5–4.5 V with baseline (c) as well as baseline and additives electrolytes (d).

reach capacity retention of at least 80% after 1000 cycles when cycled to an upper cut-off voltage of 4.2 V (corresponding to nominal 100% state of charge), our results demonstrate the immense potential of the Ni-rich NCM cathode materials when operated at higher cell voltages.

To extract an even higher capacity from the NCM811 cathodes, we increased the upper cut-off voltage to 4.5 V. A significantly higher specific capacity is achieved compared with the cell cycled to 4.35 V, i.e. 180 mAh/g vs. 160 mAh/g. The graphite/NCM811 cell using both LiDFOB and TMSPi additives delivers capacity retention of 85% after 300 cycles, while the cell using the baseline electrolyte with only a TMSPi additive just reaches retention of 66% and 73%, respectively. Moreover, the cell using LiDFOB and TMSPi also shows a higher capacity than the cell using only LiDFOB (152 mAh/g vs. 136 mAh/g), although the capacity retention is comparable (85% vs. 86%). It is worth noting that the decreased and increased capacity of the cell using a LiDFOB additive would be ascribed to the oxalate-containing salt decomposition and benign-CEI formation, respectively [22,37,38]. The related charge/discharge curves from the 1st cycle to 300th cycle are shown in Fig. 2c and d and confirm the more rapid increase in the polarization in the cell using the baseline electrolyte. The combination of LiDFOB and TMSPi additives can thus be accounted for the enhanced cycling performance as they help reduce the polarization of the cells, stabilize the cathode/electrolyte interface, and maintain a high reversible capacity. In order to further evaluate the cyclability of the cell using the baseline electrolyte with and without additives, the rate capability of the graphite/NCM811 full cells was tested in the voltage range of 2.5–4.5 V. In Fig. S3, all cells show a similar capacity at the current density of 0.1C–0.5C, while the cells using both additives display a relatively higher capacity and more stable cycling at a rate of 1C and 2C. Thus, the cell using both additives delivers a better rate capability at a high current density, although the high mass loading cathode has negative effect on the rate capability of all cells.

The cycling performance at 60 °C is shown in Fig. 3. The capacity retention suffers due to the faster kinetics of parasitic reactions at elevated temperatures. In Fig. 3a, the cell with the baseline electrolyte, with TMSPi only or with LiDFOB only, shows capacity retentions of 61%, 60%, and 77% after 100 cycles when cycled to an upper cut-off voltage of 4.35 V, while the cell with both additives shows still relatively high capacity retention of 80% under the same conditions. However, when cycled to a 4.5 V upper cut-off voltage at 60 °C, all cells show relatively poor cycling performance, regardless of if they contain additives or not. Nevertheless, the cell with both additives retains capacity retention of 71% after 100 cycles, while for the cell with individual or without the electrolyte additive, the capacity retention drops to 52%, 44% and 29%, respectively, under the same conditions (Fig. 3b). The better cycling capability of the cell combining the LiDFOB and TMSPi additives is probably ascribed to the robust CEI layer formation, which is beneficial to suppress the interphase side reaction and maintain the cathode's surface structural integrity.

The evolution of the cell impedance as determined by operando electrochemical impedance spectroscopy is an important indicator for quantifying the state of health of lithium-ion battery cells. In Fig. 4a–c, the cells with both electrolyte additives (LiDFOB and TMSPi) show a slower increase in the impedance from the 1st cycle to the 500th cycle than the cells without electrolyte additives regarding the electrode/electrolyte interphase layer impedance (R_{sf}) and charge-transfer impedance (R_{ct}) in Fig. 4d–f. Moreover, the cell with electrolyte additives displays very stable cell impedance when cycled to an upper cut-off voltage of 4.5 V, while the cell without electrolyte additives shows a dramatic increase especially from the 100th cycle to the 300th cycle in Fig. 4d–f. The full impedance spectra variations from the 1st to the 300th/500th cycle are provided in Figs. S4–5, indicating analogous trends. It is worth noting that the cell using additives displays a significantly decreased R_{ct} from the 1st to the 300th cycle, indicating that the

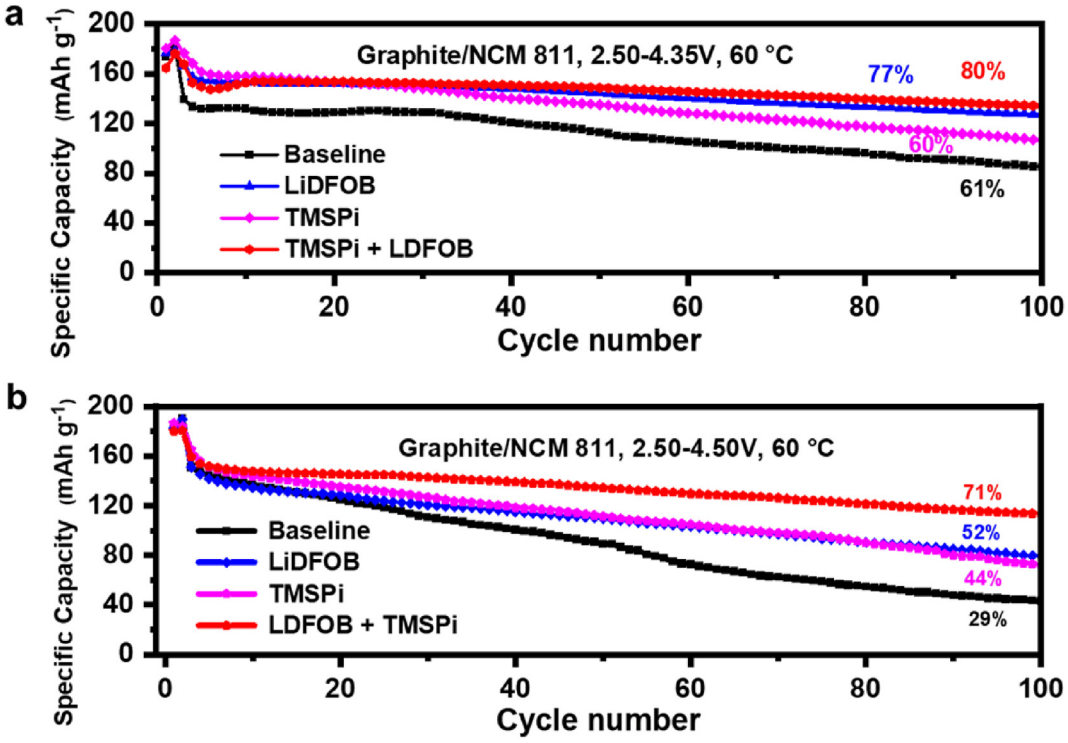

Fig. 3. The cycling performance of the graphite/NCM811 cells at an elevated temperature of 60 °C. The cells using the baseline electrolyte as well as the electrolyte with additives are cycled to an upper cut-off voltage of 4.35 V (a) and 4.5 V (b), respectively.

cell generated a robust electrode/electrolyte interphase layer, guaranteeing high interface stability and improving the cycling performance [21,36]. The extracted values of the impedance variations from the initial cycle to the 300th/500th cycle are summarized in Fig. 4g and h. The alleviated increase of the interphase layer and charge-transfer impedance plays a positive role to stabilize the electrode/electrolyte interphase and to maintain the cycling stability.

The generation of cracks in NCM cathode particles during cycling plays a crucial role in the cell performance degradation. It is known that cracks lead to a series of issues, including the formation of an additional unprotected electrode/electrolyte surface, enhancing transition metal dissolution, and apparent loss of an active material [39–41]. In Fig. 5a–c, we can clearly see the cracks formed inside of the NCM811 particles cycled in the baseline electrolyte, especially towards the top of the electrode, where the particles are located close to the separator. In a sharp contrast, hardly any cracks are visible in the NCM811 particles cycled in the electrolyte with additives as shown in Fig. 5d–f. The NCM811 particles cycled to an upper cut-off voltage of 4.5V with electrolyte additives, as shown in Fig. 5g-l, also display less cracks compared to the NMC811 particles cycled in the electrolyte without additives. The suppression of crack formation can be attributed to the formation of a robust passivating cathode electrolyte/interphase layer, which effectively releases a stress build-up and hinders crack propagation into the bulk structure, and thus mitigates and slows down the microstructural degradation [42]. To quantify a crack amount on the cycled NCM811 with and without additives, we provide a static quantity of cracks by investigating the total and cracked particles on the cycled electrode (Fig. S6). It is clear that the cell using additives just shows a 5.8% (5/86) crack ratio at 4.35V operation after 500 cycles, while the cell using the baseline shows a 28% (21/75) ratio at the same measurement. Moreover, the cell using additives displays a 19% (39/138) crack ratio at 4.5V operation after 300 cycles, while the cell using the baseline shows a ratio of 29%. Obviously, the additives effectively suppress the crack formation on the cycled NCM811, especially at 4.35V operation. The detailed working mechanism, why the additives alleviate impedance increase and crack formation, is further studied combining DFT calculations, XPS, and TOF-SIMS.

DFT calculations are performed to estimate the LUMO and HOMO of the electrolyte solvent, salt, and additive, as shown in Fig. 6a. The results show that the HOMO energy level of VC, TMSPi, and LiDFOB is much higher than that of EC and EMC. It is notable

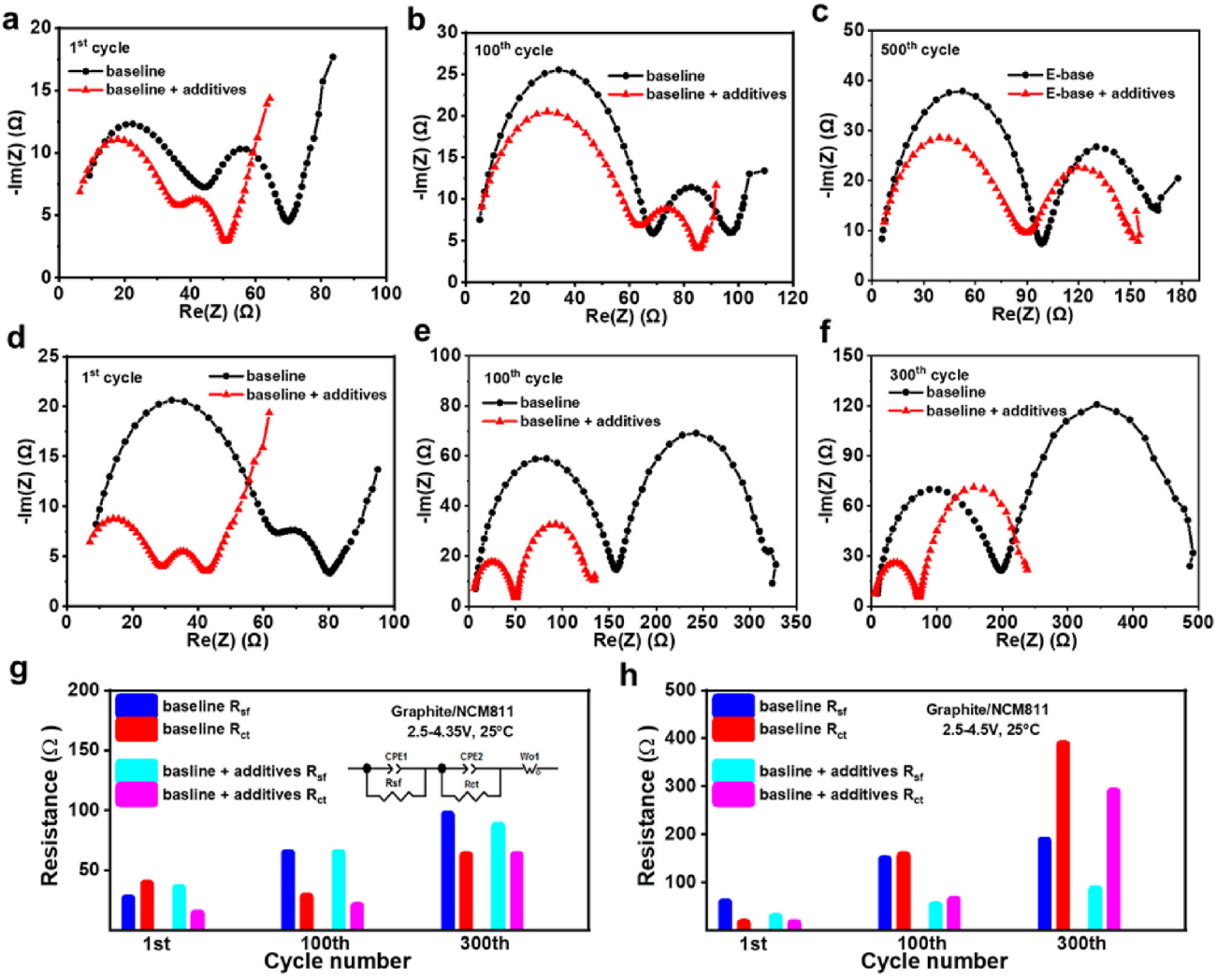

Fig. 4. Impact of electrolyte additives (LiDFOB + TMSPi) on the evolution of graphite/NCM811 cell impedance. Cells cycled to a (a–c) 4.35 V and (d–f) 4.5 upper cut-off voltage after the 1st, 100th, and 500th cycle. (g–h) The summary of impedance data (R_{sf}, R_{ct}). All operando impedance measurements were performed at a cell voltage of 4.2 V and 25 °C. LiDFOB, lithium difluoro(oxalato)borate; TMSPi, tris(trimethylsilyl)phosphite.

that the LUMO energy level of the LiDFOB is much lower than that of other components in the electrolyte followed by $LiPF_6$ and VC. The prediction matches very well with the previous work that TMSPi and LiDFOB are preferentially oxidized on the surface of the cathode as well as the LiDFOB is also preferentially reduced on the cycled graphite although the electrochemical stability limits have to be determined from the Gibbs free energy difference between the products and reagents [18,28,31,43,44]. In order to clarify why the NCM811 delivers an enhanced cycling performance at an upper cut-off voltage of 4.5 V after 300 cycles, the CEI composition was analyzed by XPS and is summarized in Fig. 6b. Relative surface composition values were extracted from the comparison of the C1s, O1s, F1s, P2p, and B1s peak areas from the photoelectron spectra measured on the electrodes cycled in the different electrolytes Fig. 6c–f. The highest ratio of Li_2CO_3 was detected on the cycled NCM811 using LiDFOB additives, while the cell using LiDFOB and TMSPi delivers the lowest ratio, which is ascribed to the decomposition of the oxalic group of LiDFOB and the synergistic effect of both additives suppressing the Li_2CO_3 formation (Fig. 6c). In Fig. 6d, the higher intensity of the M – O species was detected on the cycled NCM811 using LiDFOB and/or TMSPi than the cell using the baseline electrolyte, indicating the preferential decomposition of LiDFOB and TMSPi additives suppressing the continuous electrolyte decomposition and maintaining more the M – O (M = Ni, Co, Mn) surface, which is consistent with the DFT calculation in Fig. 6a [27,29]. Meanwhile, it is possible that no protective CEI layer formed on the surface of the NCM811 cycled in the baseline electrolyte; and therefore, the lattice O (M – O, M = Ni, Co, Mn) was broken due to the electrolyte corrosion or an incompact CEI layer covered on the surface of NCM811 and weakened the detected intensity of the M – O bond. The two possibilities are account for the lower M – O intensity on the cycled NCM811 using the baseline electrolyte. The cell using the baseline electrolyte shows a lower LiF ratio, while the cell using the LiDFOB and/or TMSPi additive delivers a higher LiF ratio in Fig. 6e. The appropriate LiF is beneficial to construct a robust CEI layer and has no obvious negative effect on the Li-ion transfer kinetics [45]. Moreover, the cell displays a higher ratio of P–O/P=O species, while the cell using TMSPi in Fig. 6f suggests that TMSPi could effectively suppress the $LiPF_6$ decomposition and the CEI-modifying ability [28]. Additionally, it is worth noting that abundant B–O species can be detected on the NCM811 cycled with LiDFOB or both LiDFOB and TMSPi additives

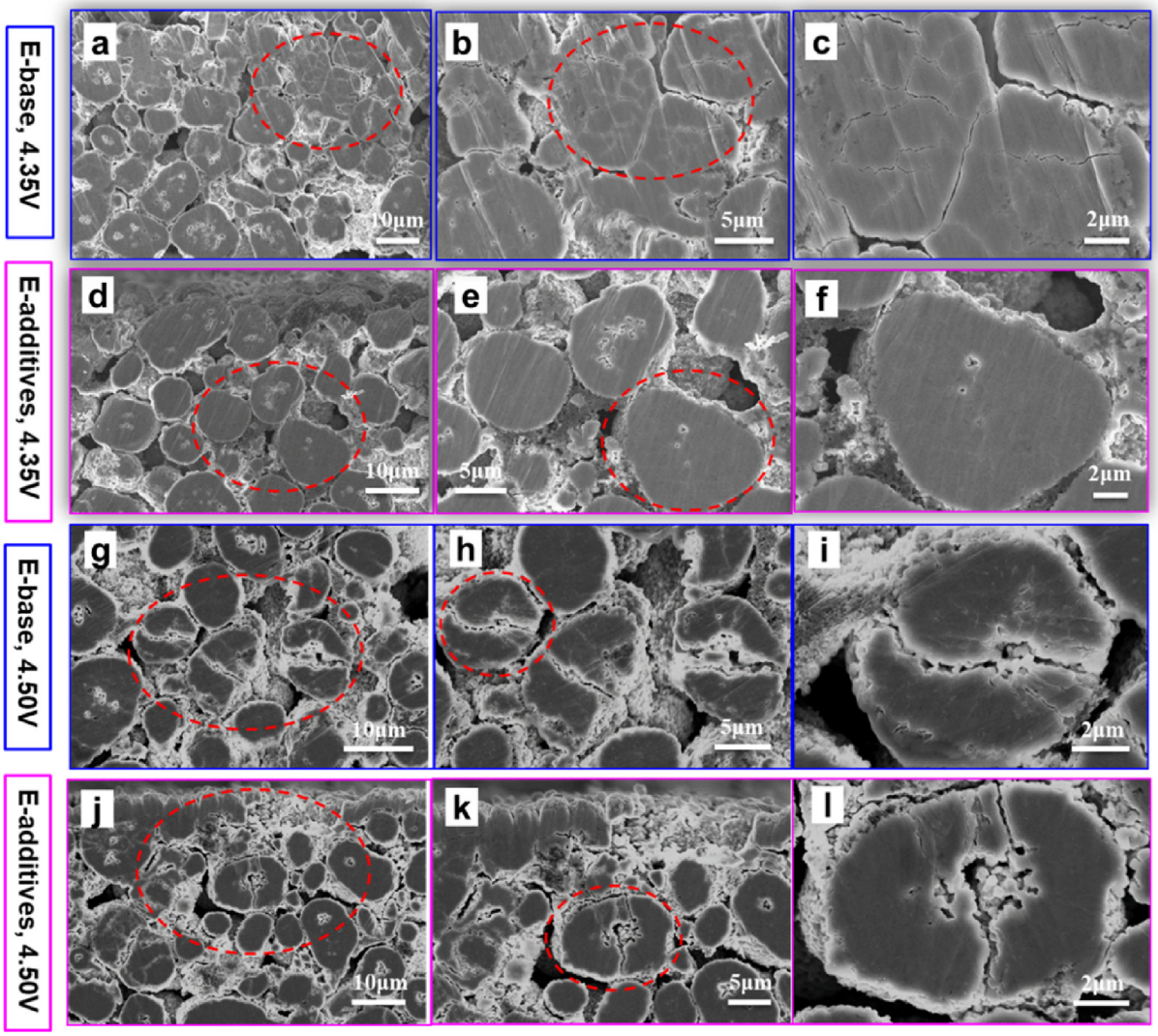

Fig. 5. Cross-section SEM images at different magnifications of the cycled NCM811 cathodes after cycling to an upper cut-off voltage of 4.35 V without (a–c) and with electrolyte additives (d–f) after 500 cycles, and corresponding images after cycling to an upper cut-off voltage of 4.5 V without (g–i) and with LiDFOB and TMSPi additives (j–l) after 300 cycles. SEM, scanning electron microscopy; TMSPi, tris(trimethylsilyl)phosphite; LiDFOB,lithium difluoro(oxalato)borate.

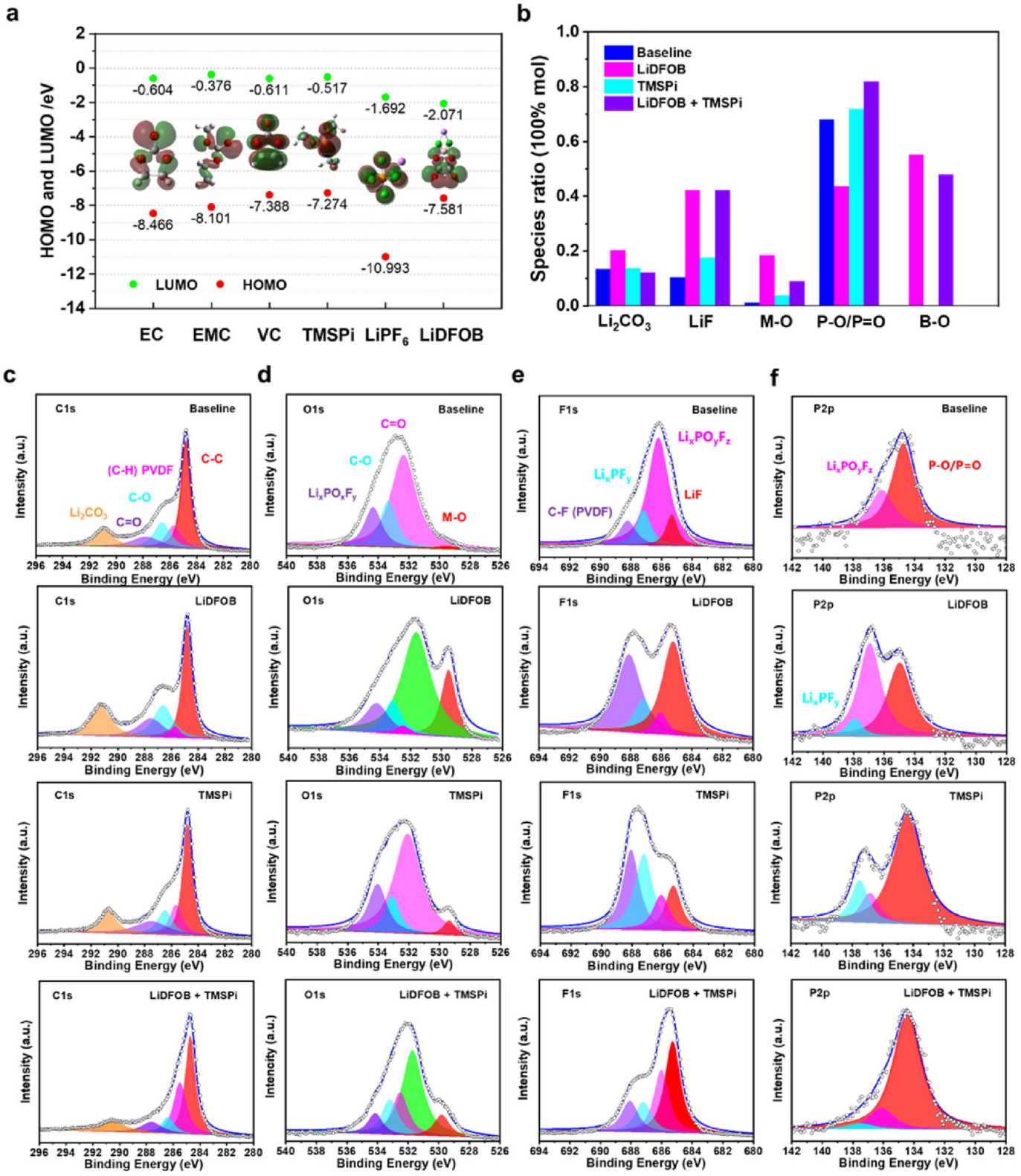

Fig. 6. prediction and detection of the interphase composition. (a) The DFT estimation of the HOMO and LUMO energy of the electrolyte components, (b) the CEI composition as determined by XPS on the cycled NCM811 electrodes, (c–f) The C1s, O1s, F1s, and P2p spectra on the cycled NCM811 after 300 cycles at 4.5V operation. XPS, X-ray photoelectron spectroscopy; DFT, density functional theory; HOMO, highest occupied molecular orbital; LUMO, lowest unoccupied molecular orbital; CEI, cathode/electrolyte interphase.

(Fig. S7), which reflects for the robustness of the CEI layer against the attack from acidic electrolyte decompositions [45]. Overall, the synergistic effort of LiDFOB and TMSPi forms a LiF-rich, B-containing, and $LiPF_6$ less-decomposed cathode/electrolyte interphase, which is beneficial to construct a robust and high-voltage tolerant CEI layer.

The transition metal dissolution is another important indicator to confirm the side reaction of the cycled NCM811 against

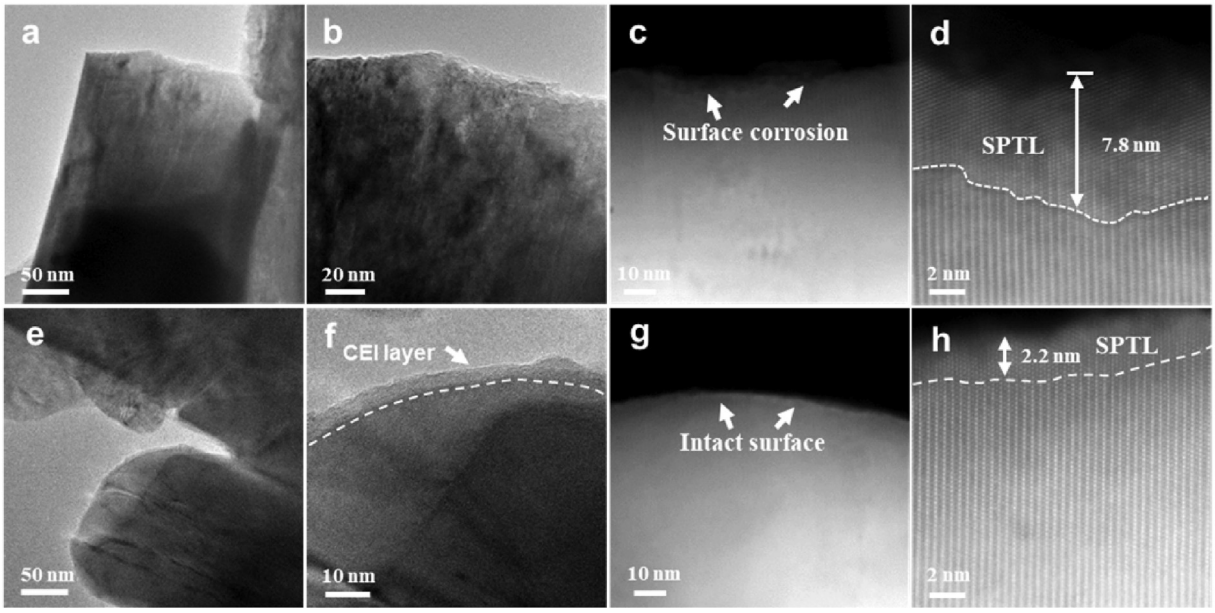

Fig. 7. cathode/electrolyte interphase (CEI) layer and surface phase transition layer as observed by TEM for the cycled in baseline electrolyte (a–b) and in the electrolyte with LiDFOB and TMSPi additives (e–f). Corresponding STEM images are shown in (c–d) and (g–h). TEM, transmission electron microscopy; STEM, scanning transmission electron microscopy; TMSPi, tris(trimethylsilyl)phosphite; LiDFOB,lithium difluoro(oxalato)borate.

electrolyte corrosion. At 4.35 V operation, Ni^+ and Mn^+ dissolution, as judged from integrated TOF-SIMS maps using electrolyte additives measured on the graphite electrodes cycled in the cell with electrolyte additives, is 3.5 times (100,400 counts vs. 30,890 counts) and 40 times lower (71,590 counts vs. 1748 counts) than that of the graphite cycled in cells without electrolyte additives, respectively (Fig. S8a). At 4.5 V operation, Ni^+ dissolution is comparable between the cycled graphite electrodes with or without additives, while Mn^+ is twice lower (68,840 counts vs. 32,960 counts) on the cycled graphite using additives (Fig. S8b). The lower transition metal dissolution strongly suggests that the additives passivate the cathode/electrolyte interface. The extracted TOF-SIMS elemental maps for Ni^+ and Mn^+ at a 4.35 V/4.5 V upper cut-off voltage with and without additives are provided in Fig. S9. An overlay map of the total species and Ni^+/Mn^+ is also shown in Fig. S10, indicating a lower coverage of Ni^+ and Mn^+ on the total species of the cycled graphite when using additives.

To understand the impact of electrolyte additives on the cathode/electrolyte interface formation after 300 cycles, TEM and high-resolution STEM were employed. In Fig. 7a, there is no visible CEI layer formed on the cycled surface using the baseline electrolyte, and there is still no visible CEI layer in the local area in Fig. 7b. This result also confirms that no CEI layer is formed during cycling or during the TEM sample preparation [41]. It is confirmed that there does not exist an intimate coating layer of CEI observed at the single-particle level in carbonate-based electrolytes even using cryogenic electron microscopy to preserve the native state and visualize the interface on positive electrodes [46]. This helps explain why a well-wrapped CEI layer is absent on the cycled cathode surface despite the widely expected intense oxidation reactions happened. Fig. 7c shows an apparent corrosion layer on the surface of cycled, which is ascribed to corrosion by fluorine ions and other acidic species resulting from electrolyte decomposition. The surface corrosion and surface phase transformation layer (SPTL) propagate into the grain bulk, as shown in Fig. 7d. The SPTL hinders the Li^+ transfer due to the formation of a disordered spinel or disordered rock salt layer, which is also detrimental for the structural integrity of the NCM811 particles and the cell's cycling stability [9,47–50]. In a sharp contrast, we can see that the CEI layer appears very clear in Fig. 7e as a layer with a weak contrast uniformly covering the surface of the cycled NCM811 in the cell cycled with electrolyte additives. In Fig. 7f, the uniform CEI layer with a thickness of 5–8 nm clearly forms on the surface of the cycled electrode due to additives decomposition, which is consistent with the DFT calculation and XPS results in Fig. 6. XPS confirms that the CEI layer consists of B-containing and LiF-enriched species, which play a critical role against a detrimental acidic species attack and in forming a robust CEI layer [19,33,50,51]. The conformal CEI layer also helps in maintaining the cathode surface stability by preventing the continuous decomposition of the electrolyte during cell cycling. Therefore, the thinner SPTL formed on the cycled using additives, guaranteeing a smooth transfer of Li^+ and thus maintaining a high reversible capacity, accounts for the significantly enhanced cycling capability of the cell using additives, as shown in Fig. 2b.

4. Conclusions

In summary, a robust and conformal CEI layer was formed by a combination of additives (2%TMSPi + 1% LiDFOB) to enable a remarkable stability of the graphite/full cell with a 24 mg/cm^2 mass loading when cycled to a 4.35 V and 4.5 V upper cut-off voltage. With the assistance of electrolyte additives, the graphite/NCM811 cell displays capacity retention of 85% after 500 cycles to 4.35 V operation, while the cell using the baseline electrolyte delivers capacity retention of 78%. The graphite/NCM811 cell using electrolyte additives further delivers excellent capacity retention of 85% after 300 cycles at an aggressive upper cut-off voltage of 4.5 V, which is far superior to the cell using the baseline electrolyte with only a 66% capacity retention. The significant improvement is attributed to the following factors: a robust LiF-rich and B-containing CEI layer, alleviated transition metal dissolution, a thinner surface phase transformation layer, and suppressed intergranular cracking in the bulk structure of the cycled NCM811. All these positive factors are derived from the synergistic oxidation of LiDFOB and TMSPi on the surface of the cycled NCM811, which forms a

robust and protective CEI layer. The electrode/electrolyte interface optimization using electrolyte additives represents a cost-effective way to suppress the continuous electrolyte decomposition during cycling and maintains a high cycling capability in graphite/NCM811 cells using electrodes with a high areal capacity. Therefore, more attention needs to be paid to the optimization of additives as an in-situ passivation strategy to boost the cycling capability and extract higher capacity via high-voltage operation.

Credit authorship statement

Wengao Zhao: conceptualization, investigation, data curation, validation, writing-reviewing and editing, and project administration. **Kuan Wang**: investigation, methodology, data curation, validation, Funding acquisition. **Romain Dubey**: investigation and resource. **Fucheng Ren**: inverstigation and software. **Enzo Brack**: investigation. **Maximilian Becker**: investigation and methodology. **Rabeb Grissa**: investigation. **Lukas Seidl**: inverstigation and methodology. **Francesco Pagani**: investigation and methodology. **Konstantin Egorov**: investigation. **Kostiantyn V. Kravchyk**: investigation and editing. **Maksym V. Kovalenko**: investigation and editing. **Pengfei Yan**: investigation and editing. **Yong Yang**: editing and supervision. **Corsin Battaglia**: supervision, editing, project administration, Funding acquisition.

Declaration of competing interest

The authors declare that they have no known competing financial interests or personal relationships that could have appeared to influence the work reported in this paper.

Data availability

Data will be made available on request.

Acknowledgments

This work was supported by InnoSuisse through funding for the Swiss Competence Center for Energy Research (SCCER) Heat and Electricity Storage under contract number 1155−002545. This work also received financial support from the National Natural Science Foundation of China (No. 12104024), China National Postdoctoral Program for Innovative Talents (BX2021024), and China Postdoctoral Science Foundation (2020M680273). We thank the Surface Science & Coating Technologies laboratory at Empa for the TOF-SIMS access.

Appendix A. Supplementary data

Supplementary data to this article can be found online at https://doi.org/10.1016/j.mtener.2023.101301.

References

[1] W.D. Li, A. Manthiram, N.M.A. High-Nickel, A colbot-free alternative to NMC and NCA cathodes for lithium-ion batteries, Adv. Mater. 32 (2020), 2002718.
[2] G.J. Chung, Y.H.T. Tran, J. Han, K. Kim, Y.S. Lee, S.-W. Song, Novel additives-package to mitigate the failure modes of high-capacity $LiNi_{0.82}Co_{0.11}Mn_{0.07}O_2$-based lithium-ion battery, Chem. Eng. J. 446 (2022), 137288.
[3] X. Fan, Y. Liu, X. Ou, J. Zhang, B. Zhang, D. Wang, G. Hu, Unravelling the influence of quasi single-crystalline architecture on high-voltage and thermal stability of $LiNi_{0.5}Co_{0.2}Mn_{0.3}O_2$ cathode for lithium-ion batteries, Chem. Eng. J. 393 (2020), 124709.
[4] R.Q. Lin, Y. Shin, R. Zhang, C.Y. Wang, K. Kisslinger, M.Y. Ge, Z. Shadike, A. Pattammattel, H.F. Yan, Y. Chu, J.P. Wu, M.S. Whittingham, H.L. Xin, X.Q. Yang, Hierarchical nickel valence gradient stabilizes high-Ni content layered cathode materials, Nat. Commun. 12 (2021) 2350.
[5] H.Y. Li, N. Zhang, Y.Q. Wang, S. Yin, H.H. Wu, J.R. Dahn, An unavoidable challenge for Ni-rich positive electrode materials for LIBs, Chem. Mater. 31 (2019) 7574−7583.
[6] R. Koerver, W. Zhang, L. de Biasi, S. Schweidler, A.O. Kondrakov, S. Kolling, T. Brezesinski, P. Hartmann, W.G. Zeier, J. Janek, Chemo-mechanical expansion of lithium electrode materials−on the route to mechanically optimized all-solid-state batteries, Energy Environ. Sci. 11 (2018) 2142−2158.
[7] S. Liu, J. Su, C. Zhang, X. Chen, J. Zhao, T. Huang, J. Wu, A. Yu, Understanding the effects of surface modification on improving the high-voltage performance of Ni-rich cathode materials, Mater, Today Energy 10 (2018) 40−47.
[8] A. Eldesoky, M. Bauer, S. Azam, E. Zsoldos, W.T. Song, R. Weber, S. Hy, M.B. Johnson, M. Metzger, J.R. Dahn, Impact of graphite materials on the lifetime of nmc811-graphite pouch cells Part I. Material properties, ARC safety tests, gas generation, and room temperature cycling, J. Electrochem. Soc. 168 (2021), 110543.
[9] W. Zhao, J. Zheng, L. Zou, H. Jia, B. Liu, H. Wang, M.H. Engelhard, C. Wang, W. Xu, Y. Yang, J.-G. Zhang, High voltage operation of Ni-rich NMC cathodes enabled by stable electrode/electrolyte interphases, Adv. Energy Mater. 8 (2018), 1800297.
[10] X.M. Fan, X. Ou, W.G. Zhao, Y. Liu, B. Zhang, J.F. Zhang, L.F. Zou, L. Seidl, Y.Z. Li, G.R. Hu, C. Battaglia, Y. Yang, In situ inorganic conductive network formation in high-voltage single-crystal Ni-rich cathodes, Nat. Commun. 12 (2021) 5320.
[11] G.L. Xu, K.S. Lau, Y.Z. Liu, X. Liu, H. Gao, X.W. Zhou, M.H. Zhuang, Y. Ren, J.D. Li, M.H. Shao, F. Pan, M.G. Ouyang, Z.H. Chen, G.H. Chen, Building ultraconformal protective layers on both secondary and primary particles of layered lithium transition metal oxide cathodes, Nat. Energy (2019) 484−494.
[12] P. Yan, J. Zheng, J. Liu, B. Wang, X. Cheng, Y. Zhang, X. Sun, C. Wang, J.-G. Zhang, Tailoring grain boundary structures and chemistry of Ni-rich layered cathodes for enhanced cycle stability of lithium-ion batteries, Nat. Energy 3 (2018) 600−605.
[13] W.G. Zhao, L.F. Zou, H.P. Jia, J.M. Zheng, D.H. Wang, J.H. Song, R. Liu, C.Y. Hong, W. Xu, Y. Yang, J. Xiao, C.M. Wang, J.-G. Zhang, Optimized Al doping improves both interphase stability and bulk structural integrity of Ni-rich NCM cathode materials, ACS Appl. Energy Mater. 3 (2020) 3369−3377.
[14] Z.H. Cui, A. Manthiram, Zinc-doped high-nickel, low-cobalt layered oxide cathodes for high energy densitu LIBs, ACS Appl. Mater. Interfaces 13 (2021) 15324−15332.
[15] Q. Xie, W. Li, A. Manthiram, A Mg-doped high-nickel layered oxide cathode enabling safer, high-energy-density Li-ion batteries, Chem. Mater. 31 (2019) 938−946.
[16] F. Schipper, H. Bouzaglo, M. Dixit, E.M. Erickson, T. Weigel, M. Talianker, J. Grinblat, L. Burstein, M. Schmidt, J. Lampert, C. Erk, B. Markovsky, D.T. Major, D. Aurbach, From surface ZrO_2 coating to bulk Zr doping by high temperature annealing of nickel-rich lithiated oxides and their enhanced electrochemical performance in lithium ion batteries, Adv. Energy Mater. 8 (2018), 1701682.
[17] X. Li, K. Zhang, M. Wang, Y. Liu, M. Qu, W. Zhao, J. Zheng, Dual functions of zirconium modification on improving the electrochemical performance of Ni-rich $LiNi_{0.8}Co_{0.1}Mn_{0.1}O_2$, Sustain. Energy Fuels 2 (2018) 413−421.
[18] X. Fan, C. Wang, High-voltage liquid electrolytes for Li batteries: progress and perspectives, Chem. Soc. Rev. 50 (2021) 10486−10566.
[19] M.Q. Xu, L.S. Hao, L.D. Xing, W.S. Li, B.L. Lucht, Investigation and application of lithium difluoro(oxalate)borate (LiDFOB) as additive to improve the thermal stability of electrolyte for lithium-ion batteries, J. Power Sources 196 (2011) 6794−6801.
[20] K. Xu, Electrolytes and interphases in Li-ion batteries and beyond, Chem. Rev. 114 (2014) 11503−11618.
[21] W. Zhao, L. Zou, J. Zheng, H. Jia, J. Song, M.H. Engelhard, C. Wang, W. Xu, Y. Yang, J.G. Zhang, Simultaneous stabilization of $LiNi_{0.76}Mn_{0.14}Co_{0.10}O_2$ cathode and lithium metal anode by lithium bis(oxalato)borate as additive, ChemSusChem 11 (2018) 2211−2220.
[22] J. Cha, J.-G. Han, J. Hwang, J. Cho, N.-S. Choi, Mechanisms for electrochemical performance enhancement by the salt-type electrolyte additive, lithium difluoro(oxalato)borate, in high-voltage lithium-ion batteries, J. Power Sources 357 (2017) 97−106.
[23] L. Madec, J. Xia, R. Petibon, K.J. Nelson, J.-P. Sun, I.G. Hill, J.R. Dahn, Effect of sulfate electrolyte additives on $LiNi_{1/3}Mn_{1/3}Co_{1/3}O_2$/graphite pouch cell lifetime: correlation between XPS surface studies and electrochemical test results, J. Phys. Chem. C 118 (2014) 29608−29622.
[24] J. Zhang, I.A. Shkrob, R.S. Assary, R.J. Clark, R.E. Wilson, S. Jiang, Q.J. Meisner, L. Zhu, B. Hu, L. Zhang, An extremely durable redox shuttle additive for overcharge protection of lithium-ion batteries, Mater. Today Energy 13 (2019) 308−311.
[25] S. Klein, P. Harte, S. van Wickeren, K. Borzutzki, S. Röser, P. Bärmann, S. Nowak, M. Winter, T. Placke, J. Kasnatscheew, Re-evaluating common electrolyte additives for high-voltage lithium ion batteries, Cell Rep. Phy. Sci. 2 (2021), 100521.
[26] J.V. Laveda, J.E. Low, F. Pagani, E. Stilp, S. Dilger, V. Baran, C. Battaglia, Stabilizing capacity retention in nmc811-graphite full cells via TMSPi electrolyte additives, ACS Appl. Energy Mater. 2 (2019) 7036−7044.
[27] H. Gao, P. Lamp, K. Amine, Z.H. Chen, Mechanistic study of electrolyte additives to stabilize high-voltage cathode-electrolyte interphase in LIBs, ACS Appl. Mater. Interfaces 9 (2017) 44542−44549.
[28] H.D. Liu, A.S. Menon, W.R. Brant, K. Edström, Understanding the roles of tris trimethylsilyl phosphite TMSPi in -Si-gr full cells, Adv. Mater. Interfac. 7 (2020), 2000277.

[29] Y.-M. Song, J.-G. Han, S. Park, K.T. Lee, N.-S. Choi, A multifunctional phosphite-containing electrolyte for 5 V-class $LiNi_{0.5}Mn_{1.5}O_4$ cathodes with superior electrochemical performance, J. Mater. Chem. 2 (2014) 9506–9513.
[30] Q.Y. Dong, Z.J. Cheng, Y.Y. Mao, R. Huang, F.S. Li, H.C. Dong, W. Li, H. Chen, Z.J. Luo, Y.B. Shen, X.D. Wu, Insights into the Dual Role of Lithium Difluoro(oxalato)borate additive in improving the electrochemical performance of graphite cells, ACS Appl. Energy Mater. 3 (2020) 695–704.
[31] Y. K Li, F.P. Jiao, K. Wu, The roles and working mechanism of salt-type additives on the performance of high-voltage LIBs, ACS Appl. Mater. Interfaces 12 (2020) 16298–16307.
[32] H.M.K. Sari, X. Li, Controllable cathode–electrolyte interface of $LiNi_{0.8}Co_{0.1}Mn_{0.1}O_2$ for lithium ion batteries A review, Adv. Energy Mater. 9 (2019), 1901597.
[33] M.Q. Xu, Y.N. Dong, Y.J. Chen, J. Demeaux, A.D. MacIntosh, Development of novel lithium borate additives for designed surface modification of high voltage $LiNi_{0.5}Mn_{1.5}O_4$ cathodes, Energy Environ. Sci. 9 (2016) 1308–1319.
[34] J. Zheng, P. Yan, L. Estevez, C. Wang, J.-G. Zhang, Effect of calcination temperature on the electrochemical properties of nickel-rich $LiNi_{0.76}Mn_{0.14-}Co_{0.10}O_2$ cathodes for lithium-ion batteries, Nano Energy 49 (2018) 538–548.
[35] D.P. Lu, T. Lozano, W.D. Bennett, G.L. Graff, B. Polzin, J.G. Zhang, M.H. Engelhard, N.T. Saenz, W.A. Henderson, P. Bhattacharya, J. Liu, J. Xiao, Failure mechanism for fast-charged lithium metal batteries with liquid electrolytes, Adv. Energy Mater. 5 (2015), 1400993.
[36] J. Zheng, P. Yan, D. Mei, M.H. Engelhard, S.S. Cartmell, B.J. Polzin, C. Wang, J.-G. Zhang, W. Xu, Highly stable operation of lithium metal batteries enabled by the formation of a transient high-concentration electrolyte layer, Adv. Energy Mater. 6 (2016), 1502151.
[37] X. Li, J. Zheng, M.H. Engelhard, D. Mei, Q. Li, S. Jiao, N. Liu, W. Zhao, J.G. Zhang, W. Xu, Effects of imide-orthoborate dual-salt mixtures in organic carbonate electrolytes on the stability of lithium metal batteries, ACS Appl. Mater. Interfaces 10 (2018) 2469–2479.
[38] L. Zou, W. Zhao, Z. Liu, H. Jia, J. Zheng, G. Wang, Y. Yang, J.-G. Zhang, C. Wang, Revealing cycling rate-dependent structure evolution in Ni-rich layered cathode materials, ACS Energy Lett. 3 (2018) 2433–2440.
[39] H. Dong, M. Xie, M. Cai, H. Liu, Z. Zhang, B. Ye, P. Zhao, W. Dong, F. Huang, Amorphous fluorine glaze for crack-free nickel-rich layered cathode grains under electrochemical cycling, Chem. Eng. J. 436 (2022), 135227.
[40] H. Zhao, Y. Bai, H. Jin, J. Zhou, X. Wang, C. Wu, Unveiling thermal decomposition kinetics of Single-Crystalline Ni-Rich $LiNi_{0.88}Co_{0.07}Mn_{0.05}O_2$ cathode for safe Lithium-Ion batteries, Chem. Eng. J. 435 (2022), 134927.
[41] W. Zhao, L. Zou, L. Zhang, X. Fan, H. Zhang, F. Pagani, E. Brack, L. Seidl, X. Ou, K. Egorov, X. Guo, G. Hu, S. Trabesinger, C. Wang, C. Battaglia, Assessing long-term cycling stability of single-crystal versus polycrystalline nickel-rich NCM in pouch cells with 6 mAh cm^{-2} electrodes, Small (2022), 2107357.
[42] W. Xue, M. Huang, Y. Li, Y.G. Zhu, R. Gao, X. Xiao, W. Zhang, S. Li, G. Xu, Y. Yu, P. Li, J. Lopez, D. Yu, Y. Dong, W. Fan, Z. Shi, R. Xiong, C.-J. Sun, I. Hwang, W.-K. Lee, Y. Shao-Horn, J.A. Johnson, J. Li, Ultra-high-voltage Ni-rich layered cathodes in practical Li metal batteries enabled by a sulfonamide-based electrolyte, Nat. Energy 6 (2021) 495–505.
[43] P. Peljo, H.H. Girault, Electrochemical potential window of battery electrolytes: the HOMO–LUMO misconception, Energy Environ. Sci. 11 (2018) 2306–2309.
[44] S.W. Mai, X.L. Liao, J.N. Hu, H.B. Lin, L.D. Xing, Y.H. Liao, X.P. Li, Tris(-trimethylsilyl)phosphite as electrolyte additive for high voltage layered lithium nickel cobalt manganese oxide cathode of lithium ion battery, Electrochim. Acta 147 (2014) 565–571.
[45] X. Fan, L. Chen, O. Borodin, X. Ji, J. Chen, S. Hou, T. Deng, J. Zheng, C. Yang, S.C. Liou, K. Amine, K. Xu, C. Wang, Non-flammable electrolyte enables Li-metal batteries with aggressive cathode chemistries, Nat. Nanotechnol. 13 (2018) 715–722.
[46] Z. Zhang, J. Yang, W. Huang, H. Wang, W. Zhou, Y. Li, Y. Li, J. Xu, W. Huang, W. Chiu, Y. Cui, Cathode-electrolyte interphase in lithium batteries revealed by cryogenic electron microscopy, Matter 4 (2021) 302–312.
[47] L.F. Zou, W.G. Zhao, H.P. Jia, J.M. Zheng, L.Z. Li, D. Abraham, G.Y. Chen, J. Croy, J.-G. Zhang, C.M. Wang, Direct contacting with liquid electrolyte facilitates the surface phase transition in Ni-rich layered cathode, Microsc. Microanal. 26 (2020) 3018–3020.
[48] L. Zou, Z. Liu, W. Zhao, H. Jia, J. Zheng, Y. Yang, G. Wang, J.-G. Zhang, C. Wang, Solid–Liquid interfacial reaction trigged propagation of phase transition from surface into bulk lattice of Ni-rich layered cathode, Chem. Mater. 30 (2018) 7016–7026.
[49] L.F. Zou, W.G. Zhao, H.P. Jia, J.M. Zheng, L.Z. Li, D.P. Abraham, G.Y. Chen, J.-G. Zhang, J.R. Croy, C.M. Wang, The role of secondary particle structures in surface phase transitions of Ni-rich cathodes, Chem. Mater. 32 (2020) 2884–2892.
[50] X.H. Zhang, L.F. Zou, Y.B. Xu, L.Q. Mu, Z.J. Yang, M.H. Engelhard, J.M. Kim, B.E. Matthews, C.J. Niu, C.M. Wang, H.L. Xin, F. Lin, W. Xu, Electrolyte regulating toward stabilization of cobalt-free ultrahigh-nickel layered oxide cathode in lithium-ion batteries, ACS Energy Lett. 6 (2021) 1324–1332.
[51] S. Jiao, X. Ren, R. Cao, M.H. Engelhard, Y. Liu, D. Hu, D. Mei, J. Zheng, W. Zhao, Q. Li, N. Liu, B.D. Adams, C. Ma, J. Liu, J.-G. Zhang, W. Xu, Stable cycling of high-voltage lithium metal batteries in ether electrolytes, Nat. Energy 3 (2018) 739–746.